Optical crosspoint matrix using broadband resonant switches

Optical Crosspoint Matrix Using Broadband Resonant Switches

Prometheus DasMahapatra, *Student Member, IEEE*, Ripalta Stabile, *Member, IEEE*, Abhinav Rohit, *Senior Member, IEEE*, and Kevin A. Williams, *Member, IEEE*

***Abstract*—A low loss, broadband crosspoint switch matrix using high-order resonant optical switch elements is designed, and fabricated for the first time. Multi-path routing is demonstrated for a broad range of representative paths across the circuit. Connections are assessed between eight inputs and four outputs to show losses as low as 0.9 dB per off state ring and 2.0 dB per on state ring. Analysis of the on-state and off-state transfer functions reveal switch extinction ratios exceeding 20 dB for operational bandwidths of 100 GHz for twenty-five different path combinations. Switching is implemented with thermo-optic tuning to give 100-GHz passbands and stopbands. Thermo-optic actuation with a 2-D array of on-chip microheaters allows rise and fall switching times of 17 and 4 microseconds respectively. Power penalties of less than 1.0 dB at 10 Gb/s are observed for twenty eight paths and comparable performance is observed for 40 Gb/s routing on representative paths through the switch matrix without significant signal degradation.**

***Index Terms*—Silicon on insulator, photonic integrated circuits, optical resonators, optical switch.**

I. Introduction

RING Resonators have been widely researched as filters, modulators, and switches [1]–[23]. The possibility for integrating large numbers of ring resonators on the same substrate is extremely promising for scalable integrated switch matrices. Much of the early research has focused on single order ring resonators (see Table I), but an inherent trade-off between the passband width and the signal extinction leads to an unacceptable compromise for broadband and high-connection count switch matrices [4]. The direct dependence of operational wavelength on waveguide dimensions has also proved incredibly challenging: Nanometer scale variations in waveguide core thickness and waveguide widths translate directly into comparable errors in peak resonance wavelengths [4]–[7]. Even for high precision Silicon on Insulator circuits fabricated in CMOS foundries, nanometer scale dimensional errors lead to considerable wavelength errors.

High-order coherently-coupled ring resonators offer an interesting route to both decouple the dependence of pass-bandwidth on extinction ratio and to relax wavelength registration requirement through a broadened passband [8]. Fifth-order ring resonators have recently been proposed as wavelength independent switches. Using an external laser source for thermo-optic switch actuation, a 300-GHz bandwidth, 17-dB extinction ratio switch has been demonstrated with low penalty 40-Gb/s routing [22].

Recently we have implemented fifth order switch elements in 1-D and 2-D arrays to explore scalable optical switch fabrics [9], [10]. The higher order elements are predicted to allow improved resilience to fabrication variations [4], [8]. We have integrated the microheaters directly above the resonators to allow direct electronic programming of the optical switch states.

In this paper we present the highest connectivity crosspoint switch matrix and analyze performance between eight inputs and four outputs. We place our work in context with a review of the state of the art for optical circuits using ring resonators as the enabling elements in Section II. We present our optical crosspoint matrix and outline the design and implementation of the circuit in Section III. Section IV describes the experimental assessment of the underlying switch element and compares the operating characteristics with a transfer matrix description of the resonant element to provide quantitative insight into the operating mechanism. In Section V, the performance for twenty-eight physical connections is experimentally assessed. Section VI studies data routing at 10 Gb/s and 40 Gb/s. The prospects for scaling to higher number of connections are subsequently discussed in Section VII.

II. State of the Art

Key advances in ring resonator circuit implementations are summarized in Table I to place our work in the context of the state of the art. Highlights are sequenced in terms of the number of coupled resonators, ranging from the simplest single order designs through to sixth order ring resonators. While higher order concepts have also been explored, these have been for delay line applications [24] rather than switching and routing. Comparisons are made in terms of the connectivity of the fabricated circuit using the $n \times m$ terminology to denote the number of physical inputs n and outputs m in the circuit. A distinction is made between single elements and arrays of elements to reflect the varying levels of circuit complexity. While the majority of published work has focused on single switch elements [14], [17]–[19], [22], [23], crossbar [9], [11], [13], [16], [21] and serpentine [1], [12], [15] architectures have also been implemented. Single and higher order elements have also been considered for these two forms of switching and routing circuits. The crossbar approach implements the resonant

Manuscript received October 7, 2013; revised December 3, 2013; accepted December 17, 2013. Date of publication February 10, 2014; date of current version May 13, 2014. This work was supported by the STW foundation project number: 11377.

P. DasMahapatra, R. Stabile, and K. A. Williams are with the COBRA Research Centre, ECO Group, Department of Electrical Engineering, Eindhoven University of Technology, 5612AZ, Eindhoven, The Netherlands (e-mail: p.dasmahapatra@tue.nl; r.stabile@tue.nl; k.a.williams@tue.nl).

A. Rohit is with PhotonIC Corp., Culver City, CA 90230 USA (e-mail: rohit@photonic-corp.com).

Color versions of one or more of the figures in this paper are available online at http://ieeexplore.ieee.org.

Digital Object Identifier 10.1109/JSTQE.2013.2296746

TABLE I
STATE-OF-THE-ART CIRCUITS

Order	Ports	Circuit	Paths tested	Band-width GHz	E.R. dB	Line rate Gbps	Power penalty dB	Group
1	4×4	Serpentine	2	39	20	c.w.	-	N. Sherwood-Droz *et al,* 2008 [1]
1	8×8	Crossbar	2	100	-	c.w.	-	B.E. Little *et al,* 2000 [11]
1	4×4	Serpentine	3	39	8	3×10	1.3	A. Biberman *et al,* 2010 [12]
1	5×5	Crossbar	2	19	8	2×3.6	-	A.W. Poon *et al,* 2008 [13]
1	2×2	One element	2	13	8	6×10	1.2	B.G. Lee *et al,* 2009 [14]
1	5×5	Serpentine	8	38	16	12.5	-1.7	R. Ji *et al,* 2008 [15]
1	2×4	Crossbar	6	56	11	5	-	A.W. Poon *et al,* 2009 [16]
1	1×2	One element	1	13	14	2.5	-1.4	A. Melloni *et al,* 2004 [17]
1	1×2	One element	1	13	14	10	2.2	A. Melloni *et al,* 2004 [17]
2	1×2	One element	1	7 [a]	14	2.5	-1.6	A. Melloni *et al,* 2004 [17]
2	1×2	One element	1	7 [a]	14.5	10	1.3	A. Melloni *et al,* 2004 [17]
3	1×2	One element	1	88 [a]	8	c.w.	-	T. Barwicz *et al,*2004 [19]
3	1×3	Series coupled	3	40	30	c.w.	-	M.A. Popovic *et al,* 2006 [20]
3	8×4	Crossbar	4	75	30	c.w.	-	S.J. Chang *et al,* 2008 [21]
5	1×2	One element	1	300	17	40	0.3	Y. Vlasov *et al,* 2008 [22]
5	1×4	Crossbar	4	100	20	10	0.3	A. Rohit *et al,* 2012 [9]
6	1×2	One element	1	102	50	c.w.	-	A. Canciamilla *et al,* 2010 [23]

E.R.: Extinction ratio.
c.w.: Continuous wave input signal.
[a]1-dB bandwidth.

switch at the intersect of orthogonal waveguides to increase the connectivity. The serpentine architecture allows the waveguides to bend to suit the placement of resonant circuits [1], [12], [15] with a reduced numbers of waveguide crossings [16]. Full connectivity between inputs and outputs is not possible, but 4×4 [1], [12] and 5×5 [15] implementations are highlighted as adequate for larger torus type networks. Experimental assessment of data routing for both serpentine and crossbar circuits have been restricted to a limited numbers of paths to date.

Key switching metrics such as bandwidth, extinction ratio and power penalty for routed data are also summarised in Table I. The low-order switch elements show relatively poor bandwidth and signal extinction. The values are coupled, restricting optimisation. Furthermore, the passband cannot be flattened, leading to a spectral narrowing for circuits which include more than one on-state low-order switching element. The first example of an 8×8 matrix [11] does show a wide 100-GHz bandwidth, but no switching mechanism is implemented for this example, preventing an estimate for off-state extinction. High-order resonators do allow a wide-bandwidth without compromising extinction. The sixth order element [23] offers 102-GHz bandwidth with 60-dB off state extinction, offering the best performance. Each of the six elements within the high-order resonant element are individually optimised for the demonstrated mode of operation. In other recent examples, the bandwidth has been comparable, but the extinction ratio has been lower. In the case of the optically switched fifth order element [22], only one part of the switch element is tuned. Tuning all of the resonant elements together may be expected to lead to considerably higher extinction ratios [4], [8]. The broadened spectral passband is also expected to relax the tolerance to wavelength registration errors across the circuit, offering the alluring prospect of multi-stage circuits for further bandwidth and connectivity scaling.

Routing of higher line-rate data and dynamic routing studies have only recently been reported. A range of power penalties have been observed. While the reported values for flat-topped high-order filters have generally been low, bandwidth narrowing may be the cause of some of the higher reported power penalties for single order designs. Dynamic switching has recently been studied. Lee *et al.* report 1.2-dB power penalty for the routing of 10-Gb/s data, and the comparative studies for dynamic routing using one input and two outputs and all-optical switching show a modest degradation to 3.5 dB. We have also recently performed 40-Gbps routing across one path in [10] and dynamic data routing between two inputs and one output in [25].

III. DESIGN AND FABRICATION

The crosspoint switch matrix using fifth order optical resonators is implemented on Silicon on Insulator technology.

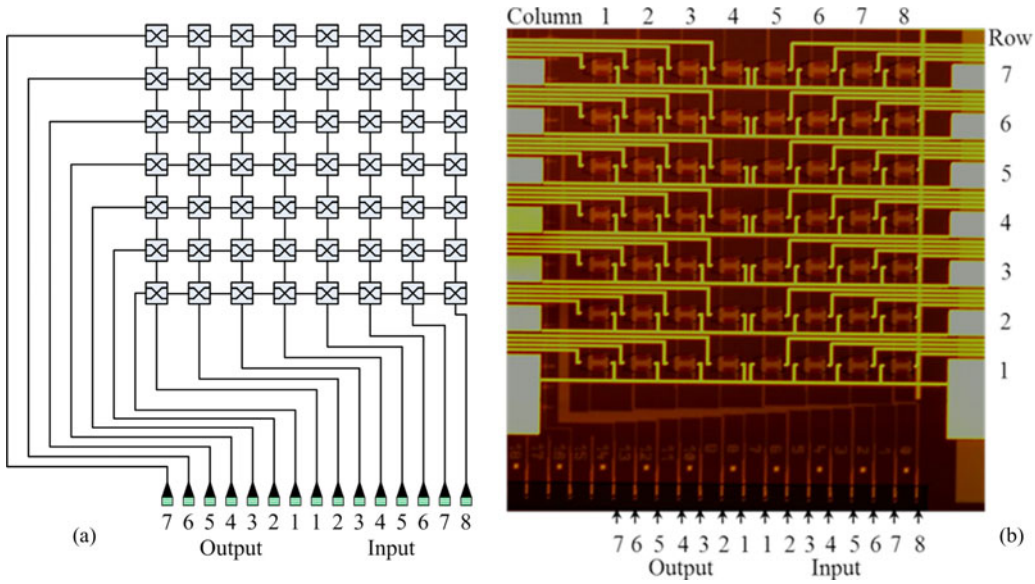

Fig. 1. (a) Schematic layout for the 8 × 7 matrix switch. (b) Photograph of the full switch matrix with seven rows of eight resonant switches in a crossbar configuration. The inputs and outputs are made via the fiber grating couplers at the bottom of the image.

Fig. 1(a) shows the schematic layout of the circuit and Fig. 1(b) shows a microscope image of the fabricated crossbar matrix of fifth order resonant switch elements. The co-fabricated micro-heaters for switching actuation are also visible on top of the resonators. These are implemented as seven rows and eight intersecting columns of waveguides. In this work, we focus on the operating characteristics for the lower four rows and therefore connections from inputs 1 through 8 to outputs 1 through 4. The optical waveguide wiring appears light and blurred as the sub-micron features are below the resolution of the optical microscope. The yellow resolved lines are the gold metal tracks to electrically connect the microheaters above the resonant switch elements. Section III-A provides details for the optical wiring design. In Section III-B the micro-heater design is outlined. The electrical addressing scheme is summarised in Section III-C.

A. *Photonic Circuit*

The photonic circuitry is fabricated on a standard silicon-on-insulator (SOI) platform by the ePIXfab foundry. The waveguide cross-section is 220 × 500 nm^2 with 1.2 μm and 2.0 μm upper and lower silica cladding respectively. The optical switch element is a fifth order ring resonator implemented with five racetrack shaped rings with bend radii of 5 μm. Fig. 2 shows in black the mask layer pattern used for the photonic wiring of one switching element. Each of the five microrings is coupled to its neighbour by a directional coupler which is defined with constant 280-nm spacing to ensure consistent reproduction of mask features across the circuit. The lengths of the couplers are 72.1 μm, 29.0 μm and 21.2 μm when moving from the external to the internal rings and define the coupling coefficients between rings. The coupling coefficients are maximised to allow an improved tolerance to fabrication variations [4] and reported in Section IV, Table II. Coupling lengths are calculated using the lightwave propagation modeling tool FimmPROP [29]. Each switch element is designed to give a free spectral range (FSR) of

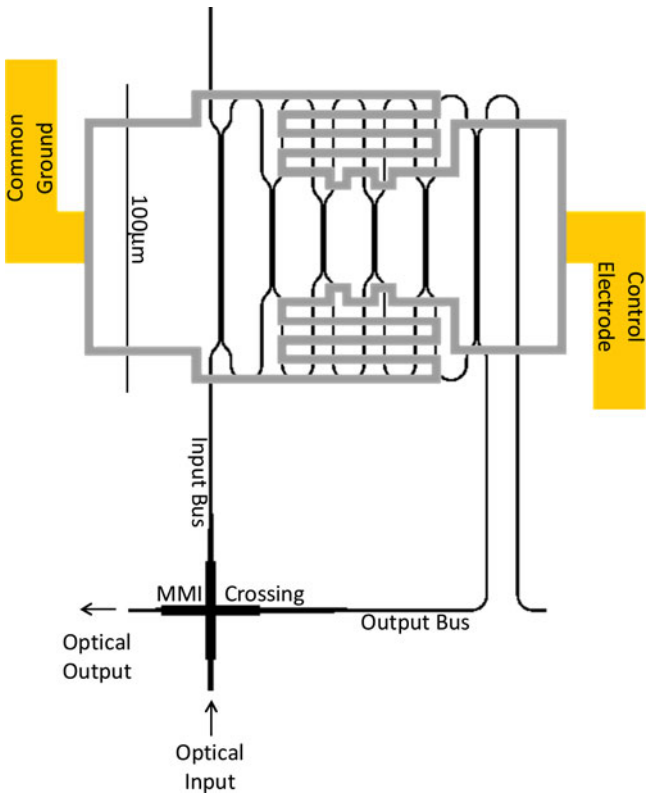

Fig. 2. Mask details for one switch element. The optical waveguides are shown in black. The narrow Ti/Pt micro-heater features are shown in grey, and the wider gold on-chip wiring is shown in orange.

350 GHz. In order to ensure a minimum desired phase shift of π, a sufficiently long ring circumference is needed. This still allows a relatively compact switch element and a sufficiently broad passband for wavelength-tolerant 40-GHz data routing [4], [8]. The input and output waveguides are densely packed and provide optical buses along the entire matrix as shown in Fig. 2.

TABLE II
PARAMETERS USED FOR TRANSFER MATRIX CALCULATIONS

Symbol	Quantity	Value
λ	Optical wavelength	1550 nm
FSR	Free spectral range	2.84 nm
κ_n	Coupling coefficient	{ 0.90, 0.60, 0.35}[a]
L	Ring circumference	200 µm
α_{fiber}	Fiber to chip coupling loss[b]	12 dB
α_{chip}	On-state chip component loss[c]	2dB
α	Optical waveguide loss	2.6 dBcm^{-1}

[a] Coupling coefficients are symmetric about the third ring.
[b] Including tapers and grating couplers.
[c] Component losses as measured in Section V-C.

They are orthogonal to each other with the input and output buses running vertically and horizontally along the chip with pitches of 300 μm and 250 μm respectively. Each switch element is located at the intersections to provide the crosspoint switch matrix architecture. Waveguide crossings are formed by 32 $\times$ 3 μm^2 multi-mode interferometers (MMI) to allow the input and output buses to cross and form the crosspoint matrix. Each switch element has a footprint area of 100 $\times$ 115 μm^2. Off-chip optical connections are achieved with a combination of one-dimensional tapers and surface grating couplers located at the bottom edge of the chip as shown in Fig. 1(a) and (b). The grating couplers operation is optimised for TE polarisation.

B. Micro-Heater Array

Two parallel 3-μm wide and 330-μm long metal micro-heaters are designed and fabricated on top of each switch element together with 18.5-μm wide metal tracks. The foundry-specified 1.2-μm thick upper silica cladding is included to separate the metal pattern from the optical waveguide core. A multi-step metallisation process is used to deposit 100-nm Ti, 20-nm Pt and 300-nm Au to form the on-chip electrical wiring. A mask pattern is used in combination with a selective gold wet-etch to remove the Au layer from the 3-μm wide micro-heater elements to obtain an enhanced parallel resistance of 400 Ω. The micro-heaters are used to locally heat up the chip to thermally tune the optical pass-band of each fifth-order resonator. The last step in fabrication involves the deposition of a polyimide passivation layer over the exposed Ti/Pt heater elements. The polyimide is removed only from the gold bond pads and the surface gratings after an exposure and development step for electrical and optical access.

C. Electrical Addressing

Each switch element is addressed by a pair of electrodes, one electrode for the control signal and an electrode for the common ground connections. One pair of micro-heater elements is used for each switch element to reduce bond-pad density and simplify control. The first four rows of the fabricated matrix—a 8 $\times$ 4 matrix—is addressed by thirty-two control electrodes.

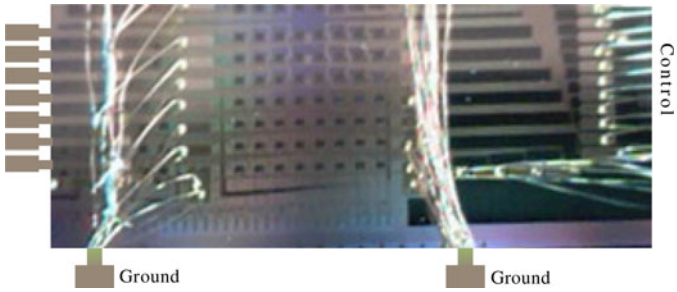

Fig. 3. Photograph of assembled circuit. Wire bonds leading to the left and right of the image are control lines. Wire bonds leading to the bottom edge are the common ground lines.

The ground connections are made separately for each row of switches, and bond-wires are led vertically off before being connected together at the heat-sink (see Fig. 3). The control-signal lines run horizontally across the width of the circuit and finally terminate at the bond pads located at the left and right chip boundaries. Bond wires are used to connect the control lines to PCBs and these are visible in Fig. 3. The entire SOI chip is epoxy-bonded to a water cooled mount and the water-chiller is maintained at a constant temperature of 22 °C.

IV. FIFTH ORDER SWITCH ELEMENT

Initial detailed switch element evaluation is performed at the intersecting switch element between row one and column one to give unambiguous pass-band and tuning data. To quantify the mode of operation, a previously described transfer matrix model [4] is used to calculate the transfer function and the tuning. To provide the most insight, the minimum parameter set is used to describe the circuit. Section IV-A outlines the parameters used, and the methodology for curve fitting. Section IV-B shows comparative measured and calculated data for the tuning response of the switch element. Section IV-C analyses the measured data in order to predict the temperature rise in the circuit.

A. Transfer Matrix Model

The frequency domain model is implemented by discritising in the periodic z-domain. The transfer function may be described in terms of the products of the optical field transfer functions for individual resonators [4], [26]:

$$\begin{bmatrix} T_N \\ R_N \end{bmatrix} = \prod_{n=0}^{N} j\left(s_n^2 \gamma_n z^{-1}\right)^{-1/2} \begin{bmatrix} 1 & -c_n \\ c_n \gamma_n z^{-1} & -\gamma_n z^{-1} \end{bmatrix} \cdot \begin{bmatrix} T_0 \\ R_0 \end{bmatrix}$$
$$c_n = \sqrt{1-\kappa_n}$$
$$s_n = \sqrt{\kappa_n}$$
$$\gamma = e^{\alpha L + j\delta\theta_n}. \quad (1)$$

The analysis describes the rings in terms of a complex propagation coefficient γ_n and a field coupling coefficients c_n and s_n. The field coupling coefficients are defined directly by the power coupling coefficent κ_n. The optical transfer function from the input to the ring coupled output may be performed for the

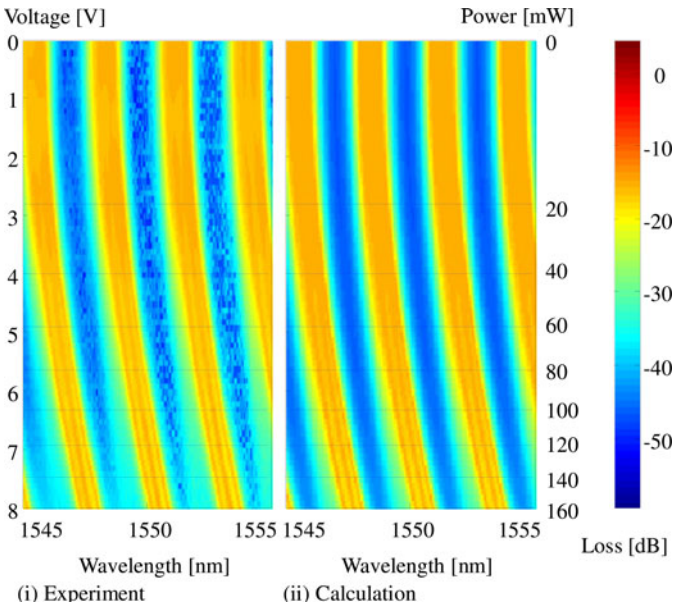

Fig. 4. Thermal tuning of the switch element connecting input 1 to output 1. Experimentally measured optical transfer functions (left) and calculated transfer functions using the transfer matrix model (right).

transmission of a normalised broadband signal from input T_0 to the output of the fifth ring at T_5. The five rings are assumed to have equal length L but different coupling and propagation coefficients. The coupling coefficients are estimated by curve fitting to the measured transfer function with no switch actuation and thus no electrical heating. The dimensions for the ring resonator are taken from the mask layout, and parameters used in the calculations are summarised in Table II.

B. Thermo-Optic Tuning

Thermo-optic tuning has been studied experimentally by recording the optical transfer function as a function of the voltage applied to the microheaters. Voltage is increased in steps of 100 mV from 0 to 8 V for the element which connects input 1 to output 1. The data are presented in Fig. 4(i) and spans across 10 nm to include three spectral ranges. A colormap is used to summarise the 81 spectral traces and emphasise the power dependence of the passband peak wavelength. The vertical axis displays the electrical input power to the microheater and assumes a constant 400-Ω resistance as the voltage increases. The tuning is superlinear with voltage and linear with electrical power, exhibiting a tuning rate of 11.8 pm/mW. A voltage change from 0 to 6.9 V (120 mW) leads to a phase tuning of 180° and two distinct switching states for the broad passbands and stopbands used. The minimum loss is denoted by the orange pass-band regions with a fiber-chip-fiber loss value of order –17 dB. The wavelength tuning is observed to be linear with electrical power. While the pass-bands are uniform at low bias, there is some evidence of increasing ripple as the tuning power increases. The stop bands are denoted in blue at a loss level of –40 to –50 dB, and here there is some speckle for the experimental data originating from the measurement noise floor. At higher electrical powers, the orange passband in the transfer function is observed to narrow and some asymmetry is introduced. This is visible as a lighter blue–green shoulder at –30 dB to the shorter wavelength side of the stop band.

TABLE III
PARAMETERS USED FOR TEMPERATURE ESTIMATIONS

Symbol	Quantity	Value
P	Heater power for π-shift	120mW
k	Thermal conductivity of Silica	0.014 $Wcm^{-1}K^{-1}$
	Thermal conductivity of Silicon	1.4 $Wcm^{-1}K^{-1}$
A_{heater}	Microheater metallisation area	$2\times10^{-5}cm^2$
A_{switch}	Optical switch element area	$1.15\times10^{-5}cm^2$
s_1	Silica upper cladding thickness	1.2 µm
s_2	Silicon waveguide core thickness	0.22 µm
s_3	Silica lower cladding thickness	2.0 µm
s_4	Silicon substrate thickness	725 µm

Calculations are performed using the transfer matrix model to isolate and quantify the origins of the passband narrowing and asymmetry at higher powers. An excess loss of 14 dB is included to match the measured and calculated data. This is consistent with the additional components and losses in the experiment. The phase tuning is varied independently for each of the modelled rings in the fifth order element. A linear dependence of phase shift on microheater power is parameterised as an electrical tuning efficiency η_n with curve-fitted values 7.4 and 13.3 pm/mW for the two outermost rings and the three innermost rings respectively. Experimental and calculated spectral characteristics show good agreement in terms of the observed pass-band narrowing, sub-structure and asymmetry. The small deviation from the ideal box-like transfer function, evident in the light blue-green shorter wavelength shoulders, can be avoided with equal tuning efficiencies for each of the five rings. This indicates that the passband distortion is an artifact of the unoptimised micro-heater design.

C. Microheater Performance

The performance of the microheater is benchmarked against the idealised case of a one-dimensional heat flux f_n. Power P flows through area A_n and leads to a temperature drop $T_{n+1} - T_n$ at layer n:

$$f_n = \frac{P}{A_n} = k_n \frac{T_n - T_{n+1}}{s_n}. \tag{2}$$

The area is defined as the microheater metallisation area for layer 1, and as the optical switch footprint area elsewhere. Equation (2) is generalised to multiple layers with a bidiagonal, thermal transfer matrix H such that $f = HT$. Interface temperatures T are then calculated, predicting a temperature rise of 122 and 69 K at the microheater and waveguide core respectively for the parameters in Table III. Notably, the temperature drop is almost halved at the waveguide core for the 1D

heatflow model and this is directly attributable to the two orders of magnitude difference in the thermal conductance for the upper silica cladding layer relative to the substrate. Ambient temperature tuning measurements [9] show an even lower 20-K temperature rise for a π phase shift. The descrepency with the ideal 1D heatflow model is attributable to the geometry of the microheaters [30]. Significant efficiency enhancements are therefore anticipated by placing the microheaters directly on the higher thermal-conductivity Silicon [30]–[32].

V. Crosspoint Matrix

The operation of the optical crosspoint matrix is studied in terms of on-state and off-state transfer functions for each path. While phase error within the high-order elements appears to be sufficiently low to give well-defined passbands, the phase error from one switch element to the next switch element leads to wavelength misalignments for non-biased resonators. As a prelude to a systematic analysis of the crosspoint matrix paths, each resonant switch element is characterised to determine the voltages required to align the passband (on state) and stopband (off state) to a common signal wavelength in Section V-A. Once these values are identified, the matrix is analysed for each path in turn with one on-state switch and the remaining switches for the path in the off-state. Representative transfer functions are presented for the on-state and off-state switch conditions in Section V-B. A comprehensive comparison of path dependent loss, operational bandwidth and switch extinction is subsequently presented for all paths in Section V-C and V-D.

A. Switch States

The on and off state bias is first determined for each switch element to enable operation at a wavelength of 1551.35 nm. The on-state is achieved when the ring-coupled passband is centred at the signal wavelength. The on-state for each path is achieved by identifying the bias voltage which leads to the flattest passband while trying to maintain a bandwidth of at least 100 GHz. The off-state bias is identified by maximising the extinction across the entire 100-GHz bandwidth.

Fig. 5 shows a plot of the on state and off state bias values as a function of the switch element. Four of the paths are untested due to open-circuits. There are some discernible similarities in terms of bias conditions for clusters of neighbouring elements, but there is also some considerable spread in the required voltages. The standard deviation of the bias for each measured on and off state is 1.3 and 0.7 V respectively. This is consistent with previous reports regarding the difficulties in precise control of resonant wavelength across circuits [9], [28]. The difference between on and off state voltage also shows comparable levels of variation with a standard deviation of 0.8 V and a mean value of 4.3 V.

To provision a path through the matrix, each switch element on the path must either be biased in the off or on state. The voltage values used are predominantly independent of the combination of paths or on-state switches selected, indicating limited thermal-crosstalk between different heater elements. For a small subset of paths however, a path dependent optimisation of the off state bias of up to 1.5 V has been performed to improve the passband flatness.

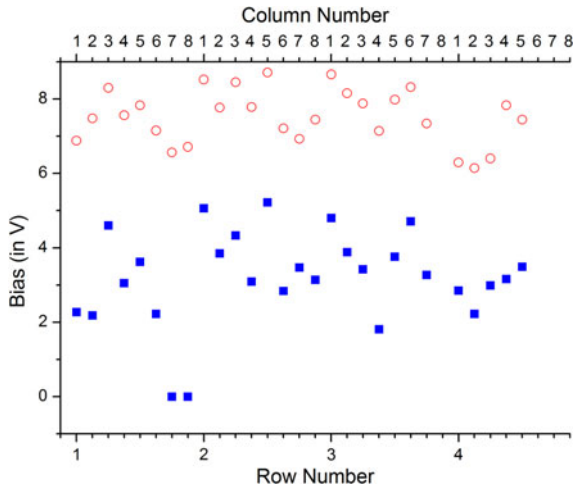

Fig. 5. On state (■) and off-state (○) voltages for an input signal centred at a wavelength of 1551.35 nm for each switch element.

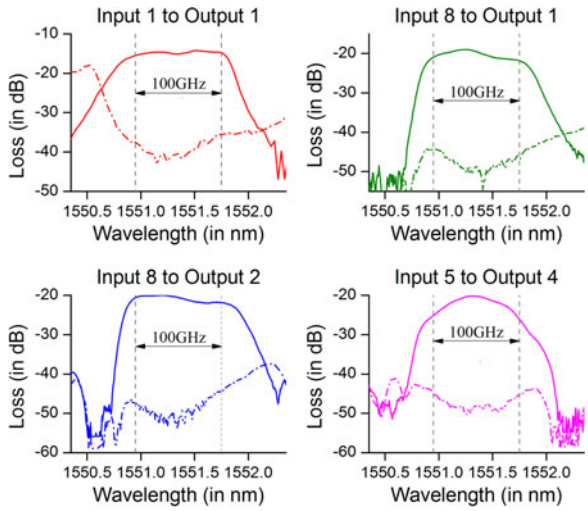

Fig. 6. On-state loss (solid) and off-state loss (dashed). The vertical dashed lines show a bandwidth of 100 GHz. A range of representative paths are presented: Shortest path from input 1 to output 1 (Red), long path from input 8 to output 1 (Green), one of the longest measured paths from input 8 to output 2 (Blue) and worst case passband from input 5 to output 4 (Magenta) are shown.

B. Optical Transfer Function

An Erbium-doped fiber amplifier is used as a broadband source at the input of the chip and the output spectrum is analysed using an optical spectrum analyser with a resolution of 0.1 nm. The spectrum is then normalized with respect to the Erbium-doped fibre amplifier (EDFA) noise spectrum in order to obtain the optical transfer function. However, the transfer function is not normalized against the grating coupler frequency response so a part of the loss exhibited in each transfer function measurement arises from the fibre-to-chip-to-fibre coupling loss which is specified to be 12 dB by the ePIXfab foundry [27], [28]. Fig. 6 shows optical transfer functions for representative switch

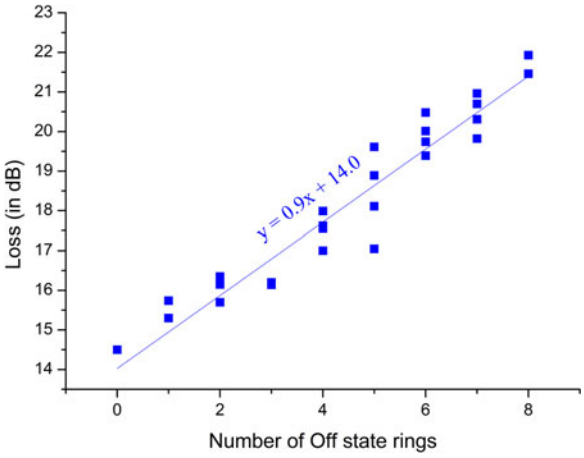

Fig. 7. Fibre coupled losses for paths through the optical switch matrix.

paths in the on and off states for input 1 to output 1, input 8 to output 1, input 8 to output 2 and input 5 to output 4.

A 100-GHz bandwidth has been marked out in Fig. 6 and across this range we obtain a signal extinction above 19 dB. While the passbands are reasonably flat, there is some path dependent ripple which may be attributable to phase error within the rings of the switch element. A slope is also observed within the passbands for some paths, and there is some asymmetry. The slope within the passband is below 3 dB for 27 of the measured paths. The slope increases to 6 dB for the switch element connecting input 5 to output 4 and this compromises the 3-dB passband, limiting it to 75 GHz. There is no clear correlation with path.

C. Optical Path Loss

Losses in the switch matrix are measured by comparing fibre to fibre losses through all the electrically measured paths. The path from input 1 to output 1 includes the fewest number of additional components with just one on state ring and no off state rings traversed. This increases to 1 on state ring and 8 off state ring components for two longest measured paths from input 8 to output 2 and from input 7 to output 3. This variation in the number of off-state switch elements allows the loss data to be used to separate common losses such as on-state switch loss and fibre chip coupling losses, from path dependent losses which include the number of crossings and off-state resonator. Fig. 7 is constructed by measuring all the losses at a wavelength of 1551.35 nm and loss data are plotted as a function of the number of off states resonant switch elements traversed. An error margin of up to 1 dB is anticipated for each measurement as a pair of fibres is scanned manually across the surface grating array. The measured losses also include waveguide propagation loss (2.6 dB/cm) and the loss for each MMI crossing (in the order of 0.1 dB [9]). A least mean square fit reveals that each off state ring incurs a loss of 0.9 dB. The intersect at 14.0 dB is expected to originate from the combination of fibre to chip losses of 2 $\times$ 6.0 dB [27], [28] and an on state ring loss of 2.0 dB.

TABLE IV
EXTINCTION RATIO ACROSS 100-GHZ BANDWIDTH

Input port	Output port (in dB)			
	1	2	3	4
1	-20.7	-20.9	-22.0	-21.4
2	-21.3	-20.7	-21.4	-21.7
3	-21.5	-21.3	-21.3	-20.2
4	-22.8	-22.7	-19.5	-23.0
5	-20.8	-21.1	-22.7	-19.5
6	-22.0	-22.5	-19.7	n.c.
7	-23.4	-20.3	-23.2	n.c.
8	-23.4	-22.3	n.c.	n.c.

n.c.: Not connected.

D. Extinction

A scalable switch fabric requires that off-state signals are maximally extinguished. The sum of contributions from the leaking off-state paths and scattering from any waveguide crossings will contribute to a path dependent crosstalk. It is not feasible to isolate the independent contributions to crosstalk in the complete circuit, so the extinction ratio for the full range of connected paths is measured.

The measured optical transfer function indicates a variation in the signal extinction achieved across the entire passband. In order to quantify extinction, the difference in extinction is spectrally resolved across a 100-GHz operation bandwidth centered at wavelength 1551.35 nm. The worst case value is recorded in Table IV. The minimum and maximum values for the lowest achievable signal extinction is 19.5 and 23.4 dB respectively.

VI. DATA ROUTING

A. Bit Error Rate Measurements

Bit error rates (BER) are measured for all the electrically connected paths. A schematic of the experimental setup is shown in Fig. 8. A tunable laser tuned to 1551.35 nm is used as input to a Mach–Zehnder modulator which is modulated at 10 Gbps using a $2^{31}-1$ pseudo-random bit sequence. The modulated pattern is then passed into the chip and the output from the chip is analysed using a XFP avalanche photo-diode receiver and a BER tester. Bit error rate is plotted as a function of receiver sensitivity for switch elements on rows 2, 4, 6, and 8 together with back to back measurements.

A plot of the BER curves for every even column element reveals minimal path independent power penalty for each measured path as shown in Fig. 9. The power penalty for all measured paths is listed in Table V with the highest power penalty of 1.0 dB for the path from input 5 to output 4 which is also the path with the highest slope in the passband.

Subsequently 40-Gbps data routing measurements are performed for a subset of paths through the circuit. A tunable laser tuned at 1543.00 nm is used as input to a Mach–Zehnder

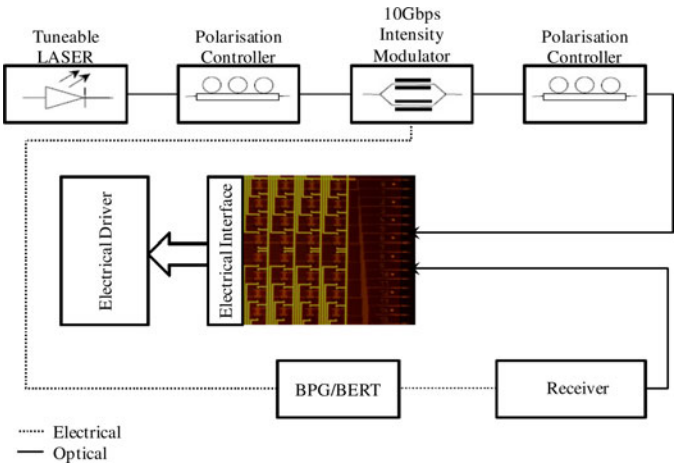

Fig. 8. Schematic of the experimental setup used for 10-Gb/s data routing.

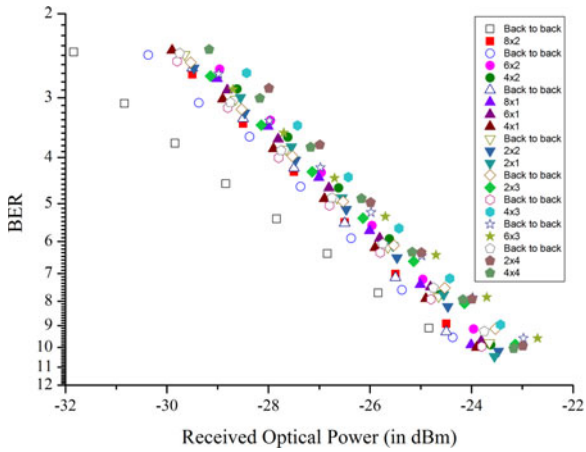

Fig. 9. Bit error rate as a function of received optical power for the even inputs to all the outputs. A 10 Gb/s 2^{31}–1 PRBS sequence is used. The solid and open symbols represent the routed and back to back measurements.

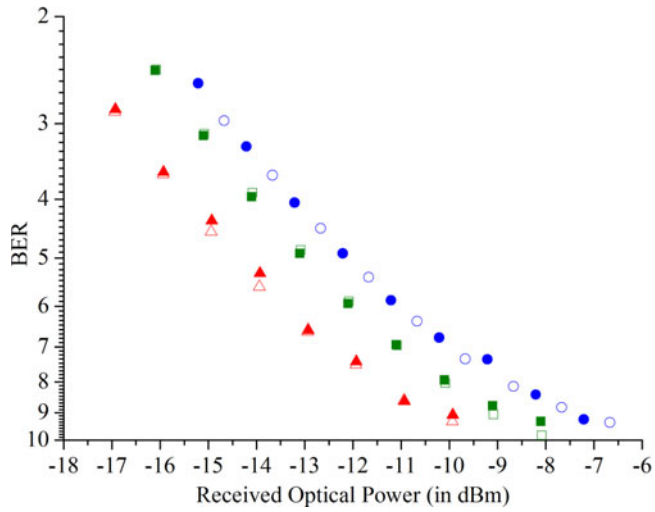

Fig. 10. Bit-error Rate curves of the measured paths at 40 Gb/s using a 2^{31}–1 PRBS sequence. The solid and open symbols represent the routed and back to back measurements for path 1 to 1 (■), 2 to 2 (▲) and 3 to 3 (●) respectively.

TABLE V
POWER PENALTY AT 10 GBIT/S

Input port	Output port (in dB)			
	1	2	3	4
1	0.0	0.0	0.1	0.4
2	0.2	0.0	0.0	0.5
3	0.2	0.4	0.4	0.5
4	0.2	0.6	0.8	0.2
5	0.1	0.7	0.6	1.0
6	0.5	0.6	0.3	n.c.
7	0.4	0.5	0.2	n.c.
8	0.3	0.3	n.c.	n.c.

n.c.: Not Connected.

modulator which is modulated at 40 Gbps using a 2^{31}–1 pseudo-random binary sequence. The modulated pattern is then passed into the chip. The output from the chip was fed into an EDFA which is filtered with a band pass filter. An SHF41210B receiver is used for this set of measurements. The received power is varied and measured after the filtered amplifier and just before the receiver. Paths from input 1 to output 1, input 2 to output 2 and input 3 to output 3 are measured as summarised in Fig. 10. Longer paths incurred too much loss for the measurement system power budget. Multiple back to back measurements are carried out by using an optical attenuator in place of the chip to account for on-chip losses and are presented along with the corresponding measurements through the chip so as to maintain a high level of consistency. Minimal power penalty is observed for each of the individual paths. Curvature in the bit-error-rate characteristics is evident in all the measurements, including the back-to-back measurements, indicating that it does not originate in the switch matrix.

B. Dynamic Routing

To evaluate the switching time associated with the switch elements, we performed multi-path dynamic routing experiments using two input ports and one output port. A 10-Gbps pattern generator was used in combination with an on-off keyed Mach–Zehnder modulator which in turn was connected to a tunable laser source tuned at 1551.35 nm. The modulated pattern was split into two with a fibre coupler and connected to two different inputs of the chip. Both the inputs were switched through the circuit to the same output port which was then visualized with a sampling oscilloscope. The trigger from the pattern generator was used to trigger the pulse generators which actuated the microheaters. Only one element is in the on-state at any particular instant of time. Input 8 and input 6 in combination with output 2 were used for the measurements. The rise and fall time are plotted in Fig. 11 and they show that the rise time is in the order of 17 μs while the fall time is in the order of 4 μs. The length of the entire pattern is 800 μs with 35 μs guard bands in between each

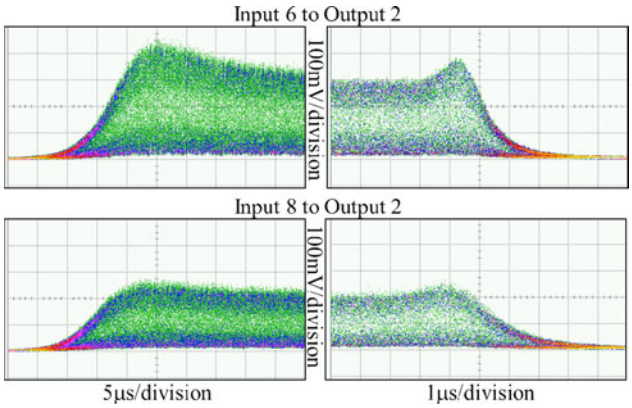

Fig. 11. Rise and fall transitions for routed 10-Gbps data for the switch elements from input 6 to output 2 (top) and input 8 to output 2 (bottom).

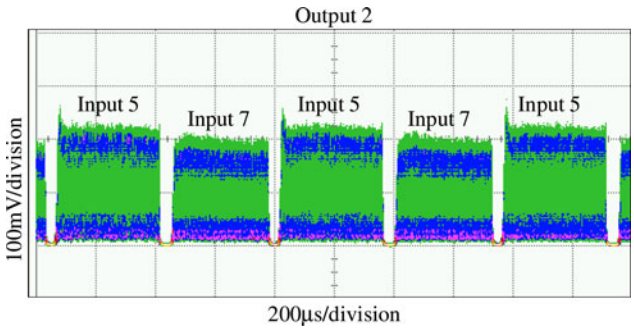

Fig. 12. 10-Gbps data routing from input 5 to output 2 and then input 7 to output 2. Input powers are normalised to minimise transients in the optical preamplifier at the receiver.

switching stage. The overshoot in the rise and fall time measurements are expected to originate from the Erbium lifetime in the fiber pre-amplifier. This is confirmed by minimising the overshoot when power leveled signals are routed to the output. Fig. 12 shows the output sequence for the case of consecutive routing from path input 5 to output 2 and input 7 to output 2 where the input signal at port 7 is deliberately attenuated to give leveled output signals. The recorded time-traces indicate a minimised overshoot.

VII. Discussion

This paper represents the largest scaling for a crosspoint switch matrix based on resonant optical elements. Further scaling in connectivity and capacity is constrained primarily by the optical losses. The dominant loss of 2 × 6 dB originates from two fibre grating couplers. Designs for fibre-chip coupling losses approaching 2 dB are now available, offering a significant performance improvement. On-chip losses appear to be dominated by the combination of the off-state by-pass losses, which may be improved with reduced waveguide losses, and also MMI crossing losses.

The 10-Gbps and 40-Gbps measurements were carried out at different resonance peaks which are separated by three FSRs. The 3-dB bandwidth of the circuit extends over 10 FSRs, allowing the prospect of high capacity routing of wavelength multiplexed data streams. Preliminary experiments have already been performed for lower connectivity circuits (see Table I). Line-rates of up to 100 Gb/s are also conceivable for the demonstrated 100-GHz bandwidth. Polarisation diversity, as recently demonstrated for a wavelength selective switch [33], may be needed however to support some of the more advanced formats.

Electrical efficiency can also be enhanced. In our heater design we achieve a π phase shift at a voltage of 6.9 V (120 mW), but the optical waveguide core is expected to be raised in temperature by a modest 20 K for a π phase shift. The application of new fabrication steps and waveguide designs to facilitate on-silicon microheaters and thermally isolated circuitry may be expected to enhance efficiency.

VIII. Conclusion

The first demonstration is presented of multi-path routing in a high connectivity optical crosspoint matrix. Fifth order resonator-based switch elements are used with losses of 0.9 dB per off state ring and 2.0 dB per on state ring. A signal extinction of 20 dB across a 100-GHz bandwidth has also been demonstrated for 25 of the 28 measured paths. Data routing experiments reveal a path independent maximum power penalty of 1.0 dB for all the measured paths with 17 and 4μs rise and fall time respectively.

Acknowledgment

The chip was fabricated in the frame of ePIXfab which has been set-up by IMEC vzw and CEA. E. Smalbrugge is acknowledged for his help in the gold etch process.

References

[1] N. Sherwood-Droz, H. Wang, L. Chen, B. G. Lee, A. Biberman, K. Bergman, and M. Lipson, "Optical 4 × 4 hitless silicon router for optical networks-on-chip (NOC)," *Opt. Exp.*, vol. 16, no. 20, pp. 15915–15922, 2008.

[2] R. A. Soref and B. E. Little, "Proposed N-wavelength M-fiber WDM crossconnect switch using active microring resonators," *IEEE Photon. Technol. Lett.*, vol. 10, no. 8, pp. 1121–1123, Aug. 1998.

[3] Q. Xu, S. Manipatruni, B. Schmidt, J. Shakya, and M. Lipson, "12.5 Gbit/s carrier-injection-based silicon micro-ring silicon modulators," *Opt. Exp.*, vol. 15, no. 2, pp. 430–436, 2007.

[4] K. A. Williams, A. Rohit, and M. Glick, "Resilience in optical ring-resonator switches," *Opt. Exp.*, vol. 19, no. 18, pp. 17232–17243, 2011.

[5] T. Barwicz, H. Byun, F. Gan, C. W. Holzwarth, M. A. Popović, P. T. Rakich, M. R. Watts, E. P. Ippen, F. X. Kärtner, and H. I. Smith, "Silicon photonics for compact, energy-efficient interconnects," *J. Opt. Netw.*, vol. 6, no. 1, pp. 63–73, 2007.

[6] W. A. Zortman, D. C. Trotter, and M. R. Watts, "Silicon photonics manufacturing," *Opt. Exp.*, vol. 18, no. 23, pp. 23598–23607, 2010.

[7] S. K. Selvaraja, W. Bogaerts, P. Dumon, D. Van Thourhout, and R. Baets, "Subnanometer linewidth uniformity in silicon nanophotonic waveguide devices using CMOS fabrication technology," *IEEE J. Sel. Topics Quantum Electron.*, vol. 16, no. 1, pp. 316–324, Jan./Feb. 2010.

[8] F. Xia, M. Rooks, L. Sekaric, and Y. Vlasov, "Ultra-compact high order ring resonator filter using submicron silicon photonic wires for on-chip interconnects," *Opt. Exp.*, vol. 15, no. 9, pp. 11934–11941, 2007.

[9] A. Rohit, R. Stabile, and K. A. Williams, "Broadband routing in a 1 × 4 SOI switch array using fifth-order resonant elements," *IEEE Photon. Technol. Lett.*, vol. 24, no. 23, pp. 2147–2150, Dec. 2012.

[10] P. DasMahapatra, A. Rohit, R. Stabile, and K. A. Williams, "Broadband 4 × 4 switch matrix using fifth-order resonators," presented at the Proc. Opt. Fiber Commun. Conf./Nat. Fiber Optic Eng. Conf., Anaheim, CA, USA, 2013, paper OW3 H.2.

[11] B. E. Little, S. T. Chu, W. Pan, and Y. Kokubun, "Microring resonator arrays for VLSI photonics," *IEEE Photon. Technol. Lett.*, vol. 12, no. 3, pp. 323–325, Mar. 2000.
[12] A. Biberman, B. G. Lee, N. Sherwood-Droz, M. Lipson, and K. Bergman, "Broadband operation of nanophotonic router for silicon photonic networks-on-chip," *IEEE Photon. Technol. Lett.*, vol. 22, no. 12, pp. 926–928, Jun. 2010.
[13] A. W. Poon, F. Xu, and X. Luo, "Cascaded active silicon microresonator array cross-connect circuits for WDM network-on-chip," in *Proc. Photon. West*, San Jose, CA, USA, 2008.
[14] B. G. Lee, A. Biberman, N. Sherwood-Droz, C. B. Poitras, M. Lipson, and K. Bergman, "High-speed 2×2 switch for multiwavelength silicon-photonic networks–on-chip," *IEEE J. Lightw. Technol.*, vol. 27, no. 14, pp. 2900–2906, Jul. 2009.
[15] R. Ji, L. Yang, L. Zhang, Y. Tian, J. Ding, H. Chen, Y. Lu, P. Zhou, and W. Zhu, "Five-port optical router for photonic networks-on-chip," *Opt. Exp.*, vol. 19, no. 21, pp. 20258–20268, 2008.
[16] A. W. Poon, X. Luo, F. Xu, and H. Chen, "Cascaded microresonators-based matrix switch for silicon on-chip optical interconnection," in *Proc. IEEE*, vol. 97, no. 7, pp. 1216–1238, jul. 2009.
[17] A. Melloni, M. Martinelli, G. Cusmai, and R. Siano, "Experimental evaluation of ring resonator filters impact on the bit error rate in non return to zero transmission systems," *Opt. Commun.*, vol. 234, no. 1–6, pp. 211–216, 2004.
[18] P. Pintus, P. Contu, N. Andriolli, A. D'Errico, F. Di Pasquale, and F. Testa, "Analysis and design of micro-ring based switching elements in a silicon photonic integrated transponder aggregator," *IEEE J. Lightw. Technol.*, vol. 31, no. 24, pp. 3943–355, Dec. 2013.
[19] T. Barwicz, M. A. Popovic, P. T. Rakich, M. R. Watts, H. A. Haus, E. P. Ippen, and H. I. Smith, "Microring-resonator-based add-drop filters in SiN: Fabrication and analysis," *Opt. Exp.*, vol. 12, no. 7, pp. 1437–1442, 2004.
[20] M. A. Popovic, T. Barwicz, M. R. Watts, P. T. Rakich, L. Socci, E. P. Ippen, F. X. Kärtner, and H. I. Smith, "Multistage high-order microring-resonator add-drop filters," *Opt. Lett.*, vol. 31, no. 17, pp. 2571–2573, 2006.
[21] S. J. Chang, C. Y. Ni, Z. Wang, and Y. J. Chen, "A compact and low power consumption optical switch based on microrings," *IEEE Photon. Technol. Lett.*, vol. 20, no. 12, pp. 1021–1023, Jun. 2008.
[22] Y. Vlasov, W. M. J. Green, and F. Xia, "High throughput silicon nanophotonic wavelength-insensitive switch for on-chip optical networks," *Nature Photon.*, vol. 2, no. 4, pp. 242–246, 2008.
[23] A. Canciamilla, M. Torregiani1, C. Ferrari1, F. Morichetti1, R. M. De La Rue, A. Samarelli, M. Sorel, and A. Melloni1, "Silicon coupled-ring resonator structures for slow light applications: Potential, impairements and ultimate limits," *J. Opt.*, vol. 12, no. 22, pp. 1–7, 2010.
[24] F. Xia, M. Rooks, L. Sekaric, and Y. Vlasov, "Ultracompact optical buffers on a silicon chip," *Nature Photon.*, vol. 1, no. 1, pp. 65–71, 2007.
[25] P. DasMahapatra, R. Stabile, A. Rohit, and K. A. Williams, "Dynamic multi-path routing in a fifth-order resonant switch matrix," presented at the Proc. Eur. Conf. Opt. Commun., London, U.K., 2013.
[26] C. K. Madsen and J. H. Zhao, *Optical Filter Design and Analysis*. New York, NY, USA: Wiley, 1999.
[27] Private communication, A. Khanna, ePIXfab coordinator, Ghent University – IMEC, Dept. of Information Technology, Sint-Pietersnieuwstraat 41 9000 Gent, Belgium, Technicum, 2012. e-mail: amit.khanna@intec.ugent.be
[28] P. Dumon and A. Khanna, "Foundry technology and services for Si photonics," in *Proc. Conf. Lasers Electro-Opt. Pacific Rim*, Kyoto, Japan, p. TuN2–3, 2013.
[29] Lightwave propagation modeling tool FimmProp, Photon Design, Oxford, U.K., [Online]. Available: http://www.photond.com/
[30] F. Gan, T. Barwicz, M. A. Popović, M. S. Dahlem, C. W. Holzwarth, P. T. Rakich, H. I. Smith, E. P. Ippen, and F. X. Kärtner, "Maximizing the thermo–optic tuning range of Silicon photonic structures," in *Proc. Photon. Switching*, 2007, pp. 67-68.
[31] M. R. Watts, J. Sun, C. De Rose, D. C. Trotter, R. W. Young, and G. N. Nielson, "Adiabatic thermo-optic Mach–Zehnder switch," *Opt. Lett.*, vol. 38, no. 5, pp. 733–735, 2013.
[32] G. Li, A. V. Krishnamoorthy, I. Shubin, J. Yao, Y. Luo, H. Thacker, X. Zheng, K. Raj, and J. E. Cunningham, "Ring resonator modulators in silicon for interchip photonic links," *IEEE J. Sel. Topics Quantum Electron.*, vol. 19, no. 6, p. 3401819, Nov./Dec. 2013.
[33] C. R. Doerr, L. L. Buhl, L. Chen, and N. Dupuis, "Monolithic flexible-grid 1×2 wavelength-selective switch in silicon photonics," *J. Lightw. Technol.*, vol. 30, no. 4, p. 473, Feb. 2012.

Prometheus DasMahapatra (S'13) received the Master's degree in nanoelectronics from the University of Manchester, Manchester, U.K., in 2011. He is currently working as a Ph.D. at the COBRA Research Institute, Eindhoven University of Technology, Eindhoven, The Netherlands. His research focuses on the simulation, design, fabrication, and evaluation of integrated opto-electronic devices and circuits based on Silicon-on-Insulator technology and InP active-passive integration technology.

Ripalta Stabile (M'13) received the Master's degree in electrical engineering from the Politecnico of Bari, Bari, Italy, in 2004. In 2005, she joined the Soft Matter Nanotechnology Group at NationalNanotechnology Laboratory, Lecce, Italy, where she received the Ph.D. degree in nanoscience in 2008. In 2009, she moved to COBRA Research Institute, Technical University of Eindhoven, Eindhoven, The Netherlands, where she was appointed as a Postdoctoral Researcher. She is currently with COBRA Research Institute, Technical University of Eindhoven. Her research interests include design, simulation, nanofabrication, and characterization of organic and inorganic photonic devices as well as large-scale photonic integrated circuits, mainly high-connectivity optical switches and high-capacity cross-connects. She is expert of high-speed electronic control of on-chip integrated systems.

Abhinav Rohit (SM'06) received the Erasmus Mundus M.Sc. degree in photonics (with Great Distinction), in 2006 and the Ph.D. degree from the Eindhoven University of Technology, Eindhoven, The Netherlands, in 2012. He is currently working as Photonic Design Engineer at PhotonIC Corp., Culver City, CA, USA. His research interests include design, fabrication, and evaluation of integrated wavelength agile switching architecture based on InP active–passive integration technology and silicon-on-insulator technology.

Kevin A. Williams (M'00) received the B.Eng. degree from the University of Sheffield, Sheffield, U.K., in 1991, and the Ph.D. degree from the University of Bath, Bath, U.K., in 1995. He was awarded a Royal Society University Research Fellowship at the University of Bristol, Bristol, U.K., in 1996. He moved to the University of Cambridge, Cambridge, U.K., in 2001, and was elected Fellow at Churchill College. In 2006, he received the European Commission Marie Curie Chair at the Eindhoven University of Technology, Eindhoven, The Netherlands. His research interests are in the area of integrated photonic circuits. Dr. Williams received the Vici award from the Netherlands Organization for Scientific Research (NWO), in 2011.